Full Paper

Wiley Online Library

ELECTROANALYSIS

DOI: 10.1002/elan.202060461

# Corrosion Inhibition of Mild Steel in Sulfuric Acid by a Newly Synthesized Schiff Base: An Electrochemical, DFT, and Monte Carlo Simulation Study

Mostafa H. Sliem,[a] N. M. El Basiony,[b] E. G. Zaki,[b] Mohammed A. Sharaf,[c] and Aboubakr M. Abdullah*[a]

**Abstract:** Effects of using a synthesized aminothiazole (BZ) Schiff base at different concentrations with and without the addition of 1 mM of KI on the corrosion mitigation of mild steel (MS) in 0.5 M sulphuric acid ($H_2SO_4$) solutions are studied electrochemically using direct and alternating currents (DC and AC) techniques. Besides, the adsorption and thermodynamic parameters are calculated in a temperature range of 293–323 K. Furthermore, Mott-Schottky analysis is used to study the type of oxide layer on the MS surface. Quantum chemical calculations and Monte Carlo simulation techniques are used, and both confirmed the experimental results.

**Keywords:** Mild steel · Corrosion · Inhibition · potential of zero charge (PZC) · Monte Carlo simulation

## Introduction

Iron alloys have many industrial applications, especially in the petroleum field. The problem that faces the use of iron alloys is its low corrosion resistance in acidic media [1,2]. Finding new materials that prevent or mitigate corrosion is one of the grand challenges for corrosion researchers. Organic compounds containing electron-donating centers such as O, N, S, and P and multiple bonds can form a protective layer on a metal surface by adsorption and reduce the corrosion [3,4]. The easiness of preparation and eco-friendliness increased the popularity of the Schiff's bases in the field of corrosion inhibition science [5,6]. The superior inhibition performance of Schiff bases compounds is attributed to the presence of the imine groups (–C=NH), which are high electron density centers because of the hetero atom and the presence of π-electrons [7,8]. Schiff bases form a protective film that protects the metal surface from the aggressive ions, e.g., $H^+$, which reduces the corrosion rate [9,10]. One of the most effective methods to increase organic inhibitors′ efficiency is the addition of inorganic halide ions such as $I^-$, $Br^-$, and $Cl^-$ [11,12]. These ions increase the adsorption tendency by forming interconnecting bridges between the metal surface′s charged active centers and the organic inhibitor [13,14]. Generally, synergism is a potential approach to enhance the inhibitors′ performance or reduce their injection dosage [15,16].

Meanwhile, the protective layers have electronic properties that play an essential role in corrosion protection of the underlying steel substrate. The analysis of such oxide layers in the inhibitor's and halide ions presence provides valuable information [17]. Mott-Schottky plots are commonly used to study a passive film's electronic properties, especially the point of zero charge (PZC) [18].

The objective of this work is to synthesize a Schiff base, namely, Benzylidene-(4-methyl-thiazol-2-yl)-amine (BZ) and to study its inhibition efficiency towards the corrosion of MS in a 0.5 M $H_2SO_4$ solutions using electrochemical polarization techniques at different temperatures, in the presence and absence of 1 mM of $I^-$ ions. Moreover, the electrochemical impedance spectroscopy (EIS) technique is utilized to study the inhibitor's effect on the passive layer and corrosion kinetics. Potential of zero charge of the MS surfaces in the absence the and the presence of the optimum concentration of the corrosion inhibitor without and with 1 mM of $I^-$ ions were obtained using Mott-Schottky tests. Furthermore, quantum chemical calculations and Monte Carlo simulation are done to investigate the relationship between the inhibitor's molecular structure and the corrosion inhibition efficiency.

[a] M. H. Sliem, A. M. Abdullah
Center for Advanced Materials, Qatar University, Doha P.O. Box 2713, Qatar
E-mail: bakr@qu.edu.qa
[b] N. M. El Basiony, E. G. Zaki
Egyptian Petroleum Research Institute, Nasr City 11727, Cairo, Egypt
[c] M. A. Sharaf
Department of Maritime Transportation Management Engineering, İstanbul University-Cerrahpaşa, Avcilar, Istanbul 34320, Turkey

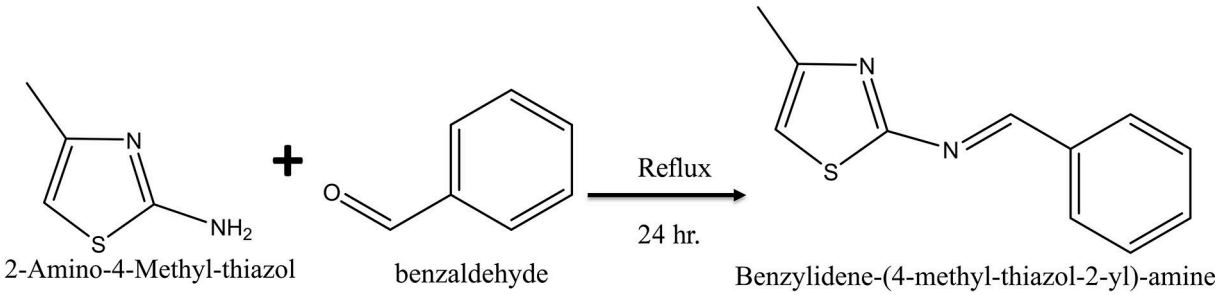


Fig. 1. Chemical structure of the Benzylidene-(4-methyl-thiazol-2-yl)-amine Schiff base

## 2 Experimental Work

### 2.1 Synthesis of the Schiff Base (BZ)

A Schiff base Benzylidene-(4-methyl-thiazol-2-yl)-amine (BZ) was prepared according to the scheme shown in Figure 1. It was synthesized by refluxing 2-Amino-4-Methyl-thiazol with benzaldehyde in a 1:1 molar ratio for 24 hr. Figure 2 shows the Fourier transform infrared (FTIR) plots of the starting and product materials to characterize the as-prepared Schiff base's functional group. It can be noticed that the disappearance of the carbonyl absorption band at 1720 $cm^{-1}$ and the appearance of the absorption band of imine group –C=N– at 1600 $cm^{-1}$ confirm the condensation reaction between the aldehyde and the amine group.

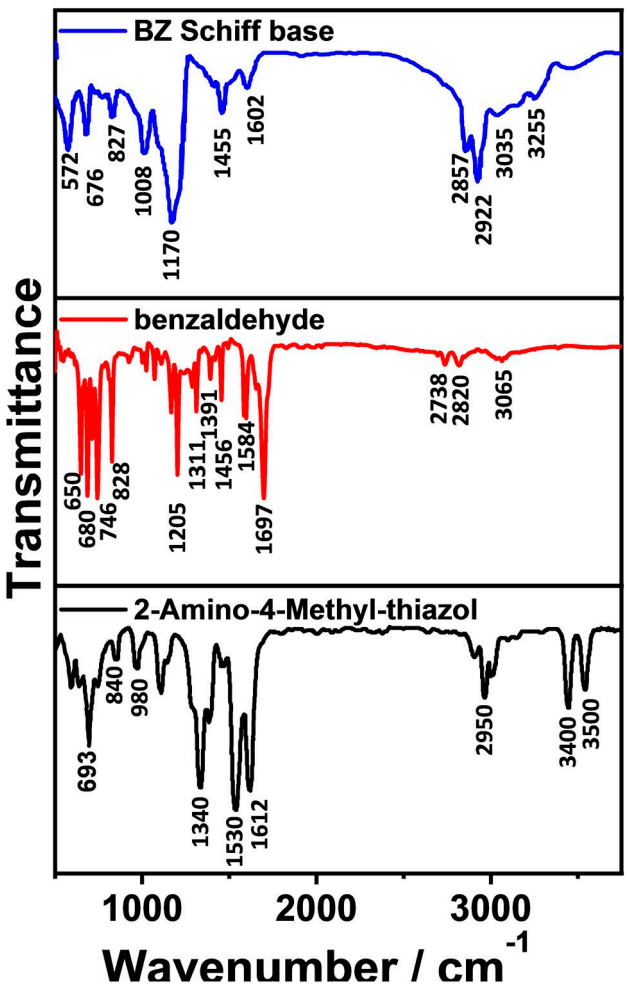


Fig. 2. FTIR spectrum of Benzylidene-(4-methyl-thiazol-2-yl)-amine Schiff base (BZ)

### 2.2 Solutions

The inhibitor solutions were mixed with 5 vol. % ethyl alcohol and then diluted with 0.5 M $H_2SO_4$. On the other hand, the corrosion behavior was tested in 0.5 M $H_2SO_4$ solution in the absence and presence of various concentrations ($5\times10^{-5}$–$1\times10^{-3}$ M) of the Schiff base and/or 1 mM KI. The 0.5 M $H_2SO_4$ solutions were prepared by the dilution of concentrated $H_2SO_4$ with deionized water. For each experiment, a freshly prepared solution is used without stirring at 298 K.

### 2.3 Electrochemical Measurement

The electrochemical measurements were carried out in a double-jacketed pyrex glass cell at room temperature using a GAMRY 3000 potentiostat/galvanostat/ZRA. The tests were designed with a three-electrode system to investigate the corrosion behavior of MS in the presence and absence of the as-prepared Schiff base using the potentiodynamic polarization and the electrochemical impedance spectroscopy (EIS) techniques. The polarization curves were measured within the potential range of ±300 mV versus the open circuit potential (OCP) with a scan rate of 0.167 mV $s^{-1}$. The potentiostatic EIS measurements were executed at OCP within a frequency range from 100 kHz to 0.01 Hz with an AC amplitude of 5 mV. EIS parameters were calculated by curve fitting of the obtained experimental data with an equivalent circuit with Echem analyst software V5.6. A Julabo F12 thermostat (GmbH, Seelach, Germany) is utilized to control the solution's temperature. All electrochemical tests were carried out at various temperatures (20, 30, 40, and 50 °C) in the inhibitor's presence and absence. The potential of zero charge for the MS surface was determined by using the Mott-Schottky approach. The capacitance measurements were performed at 100 Hz, with 50 mV applied potential shift in the negative direction. Mild steel is the

  

working electrode, whereas a graphite rod is employed as a counter electrode and a saturated calomel electrode (SCE) acts as the reference electrode in all tests. The steel specimens were purchased from Qatar steel Co., Ltd, Qatar, with an elemental composition, as shown in Table S1. The substrate samples have a cross-sectional area of 0.384 $cm^2$, which is exposed to the electrolyte. Before any experiment, the MS electrode's exposed surface area is mechanically polished using Metko FORCIPO1 V machine with silicon carbide papers of different grades (320–2500), washed roughly with acetone followed by deionized water, then dried and finally fixed into the cell. Before starting the Tafel and EIS tests, the MS electrode is placed under OCP for 30 minutes in a still deaerated solution.

### 2.4 Surface Analysis Techniques

Before and after corrosion measurements, the MS's surface morphology is examined with a scanning electron microscope (SEM, NOVANANOSEM 450) coupled with an energy dispersive X-ray (EDX) unit. A Leica DCM8 optical profilometer microscope with an intuitive 2D and 3D software offers super-fast 3D surface characterization is used to depict the 3-D surface topography of the MS and the information about the average roughness of the tested MS surfaces.

### 2.5 Theoretical Quantum Chemical Study

The theoretical quantum calculations were performed based on the density functional theory (DFT), using the MINDO3 semi-empirical method at unrestricted Hartree-Fock (UHF) level, which is included in the Hyperhem 8.0 program. The quantum calculations were computed in the gaseous and aqueous phases by considering the addition of diffuse functions for a more reliable description of the inhibition systems [19]. Additionally, the energies of the frontier molecular orbitals, such as the energy of the highest occupied molecular orbital ($E_{HUMO}$) and energy of lowest unoccupied molecular orbital ($E_{LUMO}$) are utilized to calculate different molecular parameters as reported in the equation below

$$\eta = -\frac{1}{2}(E_{HUMO} - E_{LUMO}) \tag{1}$$

$\eta$ is the global hardness, and it measures the resistance of the atom to charge transfer.

$$\sigma = 1/\eta = -2/(E_{HUMO} - E_{LUMO}) \tag{2}$$

$\sigma$ is the global softness or the hardness reciprocal, and it represents the inhibitor molecule susceptibility towards the charge transfer.

$$I = -E_{HUMO} \tag{3}$$

$$A = -E_{LUMO} \tag{4}$$

$I$ and $A$ represents the ionization potential and the electron affinity, respectively and they are sequentially related to $E_{HUMO}$ and $E_{LUMO}$

$$\chi = \frac{1}{2}(I + A) \tag{5}$$

$\chi$ is the electronegativity, and it dedicates the atom's ability to attract electrons to itself.

$$\Delta N = \frac{(\chi_{Fe} - \chi_{inh})}{2(\eta_{Fe} + \eta_{inh})} \tag{6}$$

$\Delta N$ is the fraction of electron transferred from the inhibitor molecule to the metallic atom. However, recent studies disclose that the $\chi_{Fe}$ value is not recommended as the iron Fermi energy is included in the calculation. Therefore, the Fe (110) electronegativity ($\varphi$) is emplaced instead of $\chi_{Fe}$ and the equation becomes

$$\Delta N = \frac{(\varphi - \chi_{inh})}{2(\eta_{Fe} + \eta_{inh})} \tag{7}$$

### 2.6 Monte Carlo Simulation

The corrosion inhibitor's adsorption and interactions with Fe (110) crystal surface were performed using Monte Carlo simulation with implementing the adsorption locator code in Material studio 7.0 software from Accelrys Inc., USA. Many simulation studies have been adopted the Fe (110) crystal surface as a representative system for the steel surface due to its high surface stability [20]. The simulation process was performed in a simulation box ($24.42 \times 24.42 \times 42.82$ cm) with the periodic boundary conditions to avoid any arbitrary boundary effect. The box consists of three layers. The first layer contains an iron slab with twenty layers of thickness of Fe (110) to provide an adequate depth to avoid the cut-off radius cases. The second layer contains 150 water molecules with the presence of an inhibitor molecule as well as 15 molecules of each $H_3O^+$ and $SO_4^{-2}$ ions to simulate the closest conditions to the real system. Finally, the remaining part of the box is a vacuum layer. Additionally, the COMPASS force field calculation (Condensed Phase Optimized Molecular Potentials for Atomistic Simulation Studies) was utilized for the whole simulation procedure to optimize the geometry structures for the concerned species [21].

  

## 3 Results and Discussion

### 3.1 Potentiodynamic Polarization

The corrosion potential ($E_{corr}$), corrosion current density ($i_{corr}$), the anodic and cathodic Tafel slopes ($\beta a$ and $\beta c$, respectively), the surface coverage ($\theta$), and the corrosion inhibition efficiency ($IE\%$) listed in Table 1 are obtained from the potentiodynamic polarization measurements of MS in 0.5 M $H_2SO_4$ with and without a different concentration of BZ at 20, 30, 40, and 50 °C as shown in Figure 3. It is worth mentioning that the surface coverage ($\theta$) and the inhibition efficiency ($IE\%$) are related to $i_{corr}$ values and can be estimated using the following equation: [22]

$$\theta = \frac{i_{corr} - i'_{corr}}{i_{corr}} \quad (8)$$

$$IE\% = \theta \times 100 \quad (9)$$

$i_{corr}$ and $i'_{corr}$ are the corrosion current densities before and after the addition of BZ, respectively.

It can be seen from Figure 3 at 20 °C and data in Table 1 that the values of $i_{corr}$ are inversely proportional to the BZ concentration. This indicates that the BZ molecules suppress MS's corrosion in the 0.5 M $H_2SO_4$ electrolyte [23]. The inhibition efficiency of BZ for the corrosion of MS increases with the increase of BZ. The $IE\%$ reaches its maximum (98.4 %) at a concentration of $5\times10^{-3}$ M of the BZ. Figure 3 shows the reduction in both cathodic and anodic current densities with the addition of BZ. However, the reduction in cathodic current densities is significantly more obvious than in case of the anodic ones. This, consequently, suggested that BZ acts as a mixed-type inhibitor. So, the BZ molecules are adsorbed on the MS surface, forming a protective film that impedes the dissolution of Fe and the reduction of $H^+$ ions to $H_2$ gas [24]. Moreover, cathodic Tafel curves in Figure 3 at 20 °C seem to be parallel lines, which suggest that the hydrogen evolution is activation-controlled, and the hydrogen reduction reaction mechanism does not change after the BZ addition [25].

In Figure 3, for the 20 °C plots, at anodic polarization potentials higher than −300 mV SCE, the $E$-log $i$ plots' characteristics do not change, even after the addition of various concentrations of the BZ. This potential is known as a desorption potential, at which the desorption rate of BZ molecules from the MS surface is higher than the rate of its adsorption on to MS surface. This also indicates that BZ's adsorption on the MS surface depends on the electrode potential [26]. The effect of temperature on the corrosion behavior of MS in 0.5 M $H_2SO_4$ solution in the absence and presence of different concentrations of the BZ corrosion inhibitors is also represented by the Tafel plots displayed in Figure 3. It can be noticed that the blank curves and the inhibited curves are shifted to higher current densities by elevating the temperature. This indicates that the corrosion reaction is accelerated. In Table 1, it can be seen that $i_{corr}$ increases as the temperature is raised, indicating that the corrosion rate of MS in

Table 1. Potentiodynamic polarization parameters for MS in 0.5 M $H_2SO_4$ in the absence and presence of different concentrations of BZ inhibitor at different temperatures.

| T, K | $C_{inh.}$, M | $E_{corr}$ ($mV_{SCE}$) | $i_{corr}$ ($\mu A\,cm^{-2}$) | $\beta_c$ ($mV\,dec^{-1}$) | $\beta_a$ ($mV\,dec^{-1}$) | $R_p$, $\Omega cm^2$ | *Corrosion rate*, mpy | $\theta$ | *IE*, % |
|---|---|---|---|---|---|---|---|---|---|
| 293 | Blank | −462 | 449.99 | 114.1 | 81.8 | 46.08 | 510.38 | – | – |
| | $5\times10^{-5}$ | −454 | 84.99 | 60.5 | 68.5 | 164.37 | 96.406 | 0.811 | 81.1 |
| | $1\times10^{-4}$ | −473 | 49.94 | 55.2 | 65 | 259.82 | 55.630 | 0.890 | 89.1 |
| | $5\times10^{-4}$ | −471 | 27.25 | 40.2 | 59.4 | 382.52 | 30.906 | 0.939 | 93.9 |
| | $1\times10^{-3}$ | −470 | 15.04 | 28.2 | 43.1 | 492.46 | 17.069 | 0.966 | 96.6 |
| | $5\times10^{-3}$ | −479 | 7.27 | 18.5 | 39.7 | 754.17 | 8.2511 | 0.983 | 98.4 |
| 303 | Blank | −477 | 1904.92 | 283.7 | 174.2 | 24.63 | 2160.5 | – | – |
| | $5\times10^{-5}$ | −461 | 435.31 | 160.5 | 165.7 | 81.42 | 493.71 | 0.771 | 77.1 |
| | $1\times10^{-4}$ | −486 | 371.45 | 155.1 | 156.8 | 91.26 | 421.29 | 0.805 | 80.5 |
| | $5\times10^{-4}$ | −468 | 151.51 | 101.3 | 149.5 | 173.28 | 171.83 | 0.920 | 92.0 |
| | $1\times10^{-3}$ | −490 | 80.66 | 90.2 | 138.6 | 294.50 | 91.488 | 0.957 | 95.8 |
| | $5\times10^{-3}$ | −474 | 42.22 | 46.7 | 122.8 | 348.38 | 47.888 | 0.977 | 97.8 |
| 313 | Blank | −491 | 4900.09 | 532.5 | 206.1 | 13.18 | 5557.5 | – | – |
| | $5\times10^{-5}$ | −486 | 1980.00 | 339 | 191.5 | 26.87 | 2245.6 | 0.595 | 59.6 |
| | $1\times10^{-4}$ | −488 | 1417.79 | 221.2 | 188.2 | 31.18 | 1608.0 | 0.710 | 71.1 |
| | $5\times10^{-4}$ | −453 | 721.45 | 175.4 | 168.4 | 51.77 | 818.25 | 0.852 | 85.3 |
| | $1\times10^{-3}$ | −472 | 472.34 | 169.6 | 153.2 | 74.09 | 535.72 | 0.903 | 90.4 |
| | $5\times10^{-3}$ | −463 | 234.19 | 101 | 141.5 | 109.41 | 265.61 | 0.952 | 95.2 |
| 323 | Blank | −500 | 9974.99 | 611.1 | 372.7 | 10.09 | 11313 | – | – |
| | $5\times10^{-5}$ | −502 | 7320.69 | 573 | 362.8 | 13.19 | 8302.9 | 0.266 | 26.6 |
| | $1\times10^{-4}$ | −498 | 5443.17 | 516 | 342.2 | 16.43 | 6173.4 | 0.454 | 45.4 |
| | $5\times10^{-4}$ | −490 | 3256.96 | 369.8 | 319.5 | 22.88 | 3693.9 | 0.673 | 67.3 |
| | $1\times10^{-3}$ | −481 | 1984.58 | 284.6 | 289.5 | 31.44 | 2250.8 | 0.801 | 80.1 |
| | $5\times10^{-3}$ | −472 | 1148.10 | 150.9 | 265.1 | 36.41 | 1302.1 | 0.884 | 88.5 |

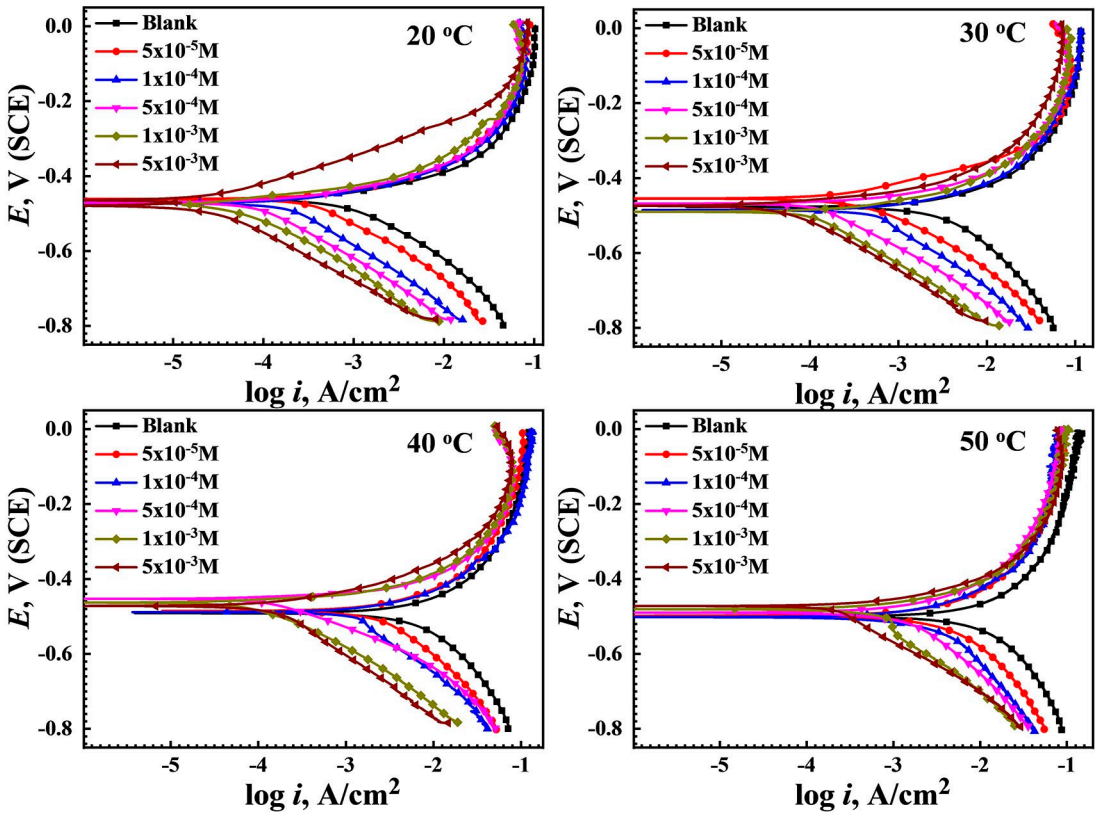


Fig. 3. Potentiodynamic polarization curves of MS in 0.5 M $H_2SO_4$ solution without and with different concentrations of BZ at 20 °C, 30 °C, 40 °C, and 50 °C. The scan rate is 0.167 mV $s^{-1}$.

0.5 M $H_2SO_4$ solution is accelerated by the increase in temperature [27]. However, compared with the blank at each temperature, $i_{corr}$ decreases significantly as the BZ inhibitor concentration increases. Therefore, despite the acceleration of corrosion rates by increasing the temperature, BZ still shows significant corrosion inhibition performance for MS in harsh environmental conditions [28].

### 3.2 Electrochemical Impedance Measurements (EIS)

In Figure 4, the Nyquist plots are displayed for the EIS measurements for MS in a 0.5 M $H_2SO_4$ solution in the absence and presence of different concentrations of the BZ corrosion inhibitor at (a) 20, (b) 30, (c) 40, and (d) 50 °C. The dots are the real data, while the solid lines are the fitted ones using the electrical one-time constant equivalent circuit shown in Figure S1. Fitting the data using the one-time constant equivalent circuit generated the charge transfer resistance $R_{ct}$ ($\Omega cm^2$), double layer capacitance $C_{dl}$ ($\mu F cm^{-2}$), solution resistance $R_s$ ($\Omega cm^2$), the surface coverage ($\theta$), and the inhibition efficiency $IE$ (%). Additionally, Figure S2 represents the Bode plots for the same data as Figure 4. The EIS parameters extracted from Figures 4 and S2 are listed in Table 2. It is worth mentioning that $\theta$ is calculated as the following equation [29].

Table 2. EIS parameters for the corrosion of MS in 0.5 M $H_2SO_4$ in the absence and presence of different concentrations of BZ inhibitor at different temperatures.

| T, K | $C_{inh}$, M | $R_S$, $\Omega cm^2$ | $R_{ct}$, $\Omega cm^2$ | $C_{dl}$, $\mu F.cm^{-2}$ | $\theta$ | $IE_{eis}$, % |
|---|---|---|---|---|---|---|
| 293 | Blank | 2.46 | 32.93 | 75.91 | – | – |
| | $5\times10^{-5}$ | 2.48 | 118.9 | 57.40 | 0.723 | 72.38 |
| | $1\times10^{-4}$ | 2.47 | 217.5 | 34.72 | 0.843 | 84.31 |
| | $5\times10^{-4}$ | 2.777 | 362.5 | 28.34 | 0.909 | 90.99 |
| | $1\times10^{-3}$ | 2.82 | 440.5 | 26.64 | 0.925 | 92.51 |
| | $5\times10^{-3}$ | 2.407 | 575.2 | 20.27 | 0.949 | 94.98 |
| 303 | Blank | 2.56 | 25.29 | 86.16 | – | – |
| | $5\times10^{-5}$ | 2.957 | 70.09 | 74.88 | 0.635 | 63.54 |
| | $1\times10^{-4}$ | 2.05 | 100.5 | 57.64 | 0.744 | 74.48 |
| | $5\times10^{-4}$ | 2.608 | 137.5 | 42.68 | 0.814 | 81.44 |
| | $1\times10^{-3}$ | 2.624 | 218.3 | 32.58 | 0.883 | 88.30 |
| | $5\times10^{-3}$ | 2.68 | 289.4 | 24.22 | 0.911 | 91.18 |
| 313 | Blank | 2.55 | 13.08 | 108.40 | – | – |
| | $5\times10^{-5}$ | 2.71 | 25.83 | 76.5 | 0.493 | 49.30 |
| | $1\times10^{-4}$ | 2.53 | 34.28 | 62.4 | 0.618 | 61.84 |
| | $5\times10^{-4}$ | 2.59 | 50.25 | 51.2 | 0.739 | 73.97 |
| | $1\times10^{-3}$ | 2.97 | 76.54 | 34.98 | 0.829 | 82.91 |
| | $5\times10^{-3}$ | 2.83 | 101.8 | 26.2 | 0.871 | 87.15 |
| 323 | Blank | 2.61 | 7.083 | 160.4 | – | – |
| | $5\times10^{-5}$ | 2.51 | 10.83 | 78.8 | 0.344 | 34.44 |
| | $1\times10^{-4}$ | 2.58 | 13.21 | 69.6 | 0.463 | 46.36 |
| | $5\times10^{-4}$ | 2.11 | 21.19 | 58.1 | 0.665 | 66.58 |
| | $1\times10^{-3}$ | 2.67 | 33.08 | 39. | 0.785 | 78.59 |
| | $5\times10^{-3}$ | 2.53 | 43.03 | 30.1 | 0.827 | 82.73 |

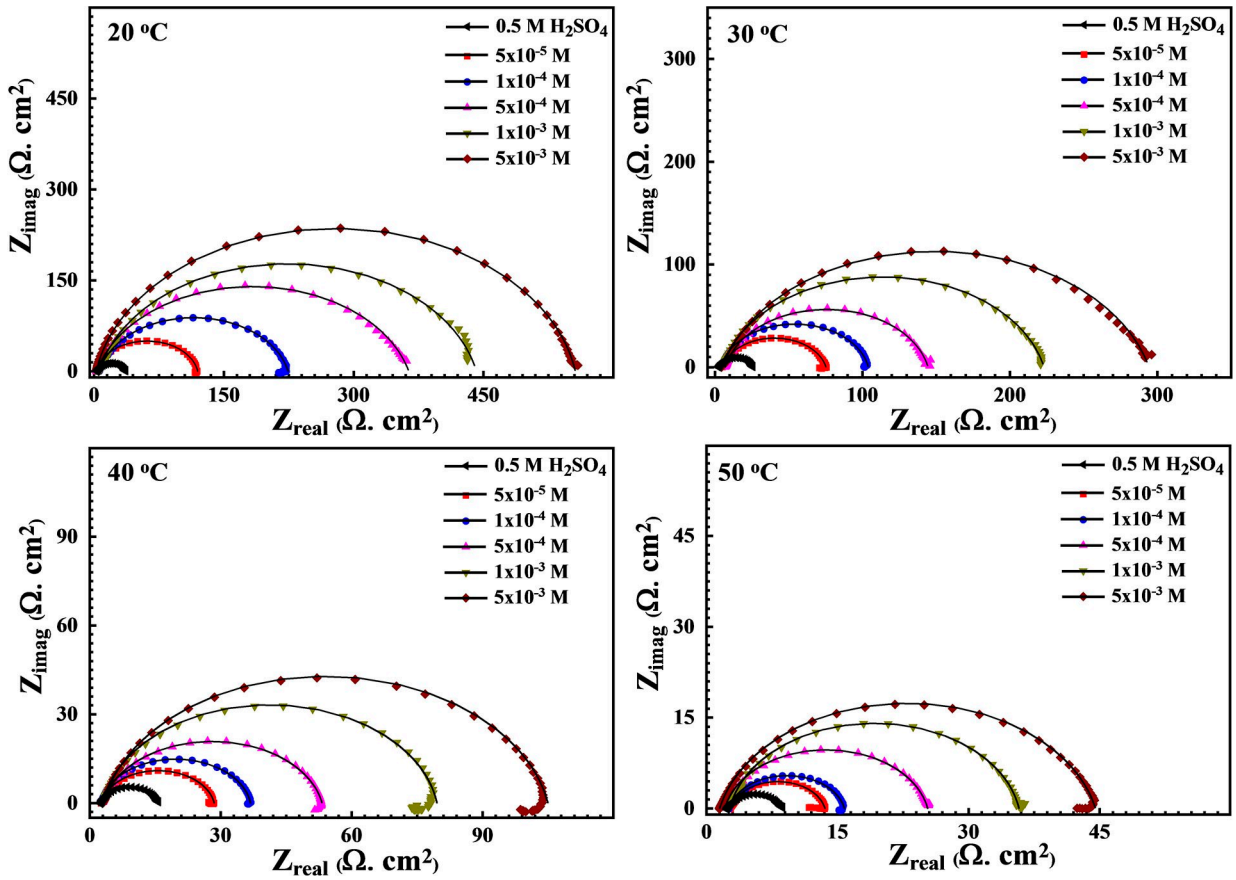


Fig. 4. Nyquist plots for MS in 0.5 M $H_2SO_4$ without and with different concentrations of BZ corrosion inhibitors at 20 °C, 30 °C, 40 °C, and 50 °C. The dots are the real data, while the solid lines are the fitted ones using the equivalent circuit shown in Figure S1. The frequency range is from 0.01 Hz to 100 kHz with an amplitude of 5 mV.

$$\theta = \frac{R_{ct2} - R_{ct1}}{R_{ct2}} \tag{10}$$

where $R_{ct1}$ and $R_{ct2}$ are the charge-transfer resistances in the absence and presence of the inhibitor, respectively.

Moreover, the corrosion inhibition efficiency ($IE\%$) was calculated using Equation 10.

The obtained results show that the $R_{ct}$ values increases, and the $C_{dl}$ values decrease as inhibitor concentration increases. The reason for this is attributed to a protective film formed on the MS/solution interface [30]. According to the Helmholtz model, the double-layer capacitance is inversely proportional to the surface changes according to Equation 4:

$$C_{dl} = \frac{\varepsilon\varepsilon_0}{\delta_{ads}} A \tag{11}$$

where $\delta_{ads}$ is the adsorbed film thickness, $A$ is the electrode surface area, $\varepsilon_0$ is the permittivity of air and $\varepsilon$ is the local dielectric constant. The decrease in $C_{dl}$ values may be referred to as the increase of the thickness of the adsorbed inhibitor molecules' film and/or due to the replacement of the adsorbed water molecules the metal/solution interface [31]. The Nyquist plots in Figure 4 for all the BZ concentrations have the same behavior, and they are all depressed semicircles. This proves that MS's dissolution reaction mechanism does not change due to the BZ corrosion inhibitor addition, and the inhibition process is controlled by the charge transfer [32,33]. It is also noted that the Nyquist plots appeared depressed at the intermediate frequency region. No perfect semicircles are observed due to the frequency dispersion phenomenon related to the electrode surface heterogeneity resulting from the roughness of the surface [34]. At intermediate frequencies, the phase angle increases in the negative direction towards −90° as the inhibitor's concentration increases, as shown in Figure S2. This reveals a more capacitive response, i.e., lower corrosion rates at higher concentrations of BZ inhibitor [35].

The listed $IE$ % data in Table 2 indicates the increasing corrosion resistance behavior of MS with increasing the BZ concentration, where the inhibition efficiency reached 95. 0 % at $5\times10^{-3}$ M of BZ at 20 °C. Meanwhile, at 30, 40, and 50 °C, a remarkable shrinkage in the diameter of the depressed capacitive loop occurs with an increase in the temperature, which reveals that the corrosion resistance of MS is decreased by the

  

temperature the $R_{ct}$ values decrease. In contrast, the $C_{dl}$ values increase with the increase in temperature [36]. Such a phenomenon may be attributed to the active thermal motion of the molecules, which boosts the desorption tendency of the adsorbed inhibitor molecules and promote the charge transfer process at the metal/surface interface. In other words, increasing the temperature decreases the surface coverage and, consequently, the corrosion inhibition efficiency [37]. The EIS data serves to confirm the polarization data.

### 3.3 Inhibitor Adsorption Isotherm Model

The corrosion inhibitor molecules′ adsorption mechanism on the metal active sites has been explained via the displacement of the solution molecules at the metal/electrolyte interface [38]. Additionally, the metal/solution interaction, whether a spontaneous or non-spontaneous reaction, even if it is chemical or physical adsorption, can be determined according to the adsorption isotherm models. Langmuir adsorption isotherm presents the best explanation for the BZ corrosion inhibitor‘s adsorption on the MS interface, as seen in the equation below [39].

$$\frac{C_{\text{inh}}}{\Theta} = \frac{1}{K_{\text{ads}}} + C_{\text{inh}} \tag{12}$$

where $C_{inh}$ is the inhibitor concentration, Θ is the surface coverage, and $K_{\text{ads}}$ is the adsorption equilibrium constant. Figure S3 signifies a straight-line relation attained from $\frac{C_{inh}}{\Theta}$ versus $C_{inh}$ at different temperatures. The intercept of the straight lines with y-axis represents the value of the $K_{\text{ads}}$ at different temperatures with a regression coefficient ($R^2 > 0.99$).

The standard adsorption free energy change value of the chemical interaction is determined using the equation below [40,41]

$$K_{ads} = \frac{1}{55.5} e^{\frac{-\Delta G^o_{ads}}{RT}} \tag{13}$$

where 55.5 is the water′s molar concentration, $R$ is the universal gas constant and equal 8.32 J mol$^{-1}$ K$^{-1}$, and $T$ is the absolute temperature (293, 303, 313, and 323 K).

From these calculations, $K_{ads}$ is directly proportional to the standard Gibbs free energy change, and the more negative $\Delta G^o_{ads}$, the higher the BZ molecules adsorbability. Additionally, the negative value of $\Delta G^o_{ads}$ assumes that the BZ molecules are spontaneously adsorbed on the MS interface [42]. Also, the strength of the bond between adsorbent and adsorbate is explained from the $K_{ads}$ values as seen in Table 3. The values of $K_{ads}$ decrease with an increase in temperature where the bond between MS and BZ molecules is weakened. Moreover, many studies have differentiated between chemisorption and physisorption processes on the basis of the $\Delta G^o_{ads}$ value. If the $\Delta G^o_{ads}$ is more negative than −40 kJ/mol, it is considered as a chemisorption process as sharing of electrons takes place between the inhibitor and the metal. Meanwhile, if the $\Delta G^o_{ads}$ is more positive than −20 kJ/mol, a physisorption process is taken into consideration where an electrostatic interaction occurred between the charged metal surface and the inhibitor [43]. From Table 3, the $\Delta G^o_{ads}$ values are in the range from −37.89 to −35.41 kJ/mole. It can be assumed that the BZ molecules adsorption on the metal surface pursues both chemisorption and physisorption processes. Furthermore, Van′t Hoff’s relationship was utilized to calculate the adsorption′s enthalpy change, as seen in the equation below [44].

Table 3. Adsorption and thermodynamic parameters from Langmuir adsorption isotherm of the BZ corrosion inhibitor on the MS surface at different temperatures.

| Temperature, K | $K_{\text{ads}}$, L mol$^{-1}$ | $\Delta G^{\circ}_{\text{ads}}$ (kJ.mol$^{-1}$) | $\Delta H^{\circ}_{\text{ads}}$ (kJ.mol$^{-1}$) | $\Delta S^{\circ}_{\text{ads}}$ (kJ.mol$^{-1}$) |
|---|---|---|---|---|
| 293 | 9983 | −37.89 | −59.74 | 74.91 |
| 303 | 3264 | −36.31 | | 77.44 |
| 313 | 1912 | −36.12 | | 75.58 |
| 323 | 955.1 | −35.41 | | 75.43 |

$$\ln K_{ads} = \frac{-\Delta H^o_{ads}}{RT} + \frac{\Delta S^o_{ads}}{R} \tag{14}$$

where $\Delta H^o_{ads}$ and $\Delta S^o_{ads}$ are the standard enthalpy and the entropy changes of the adsorption process, respectively.

Figure S4 depicts a straight line from the relation between ln $K_{\text{ads}}$ versus 1/T and from the slop and the intercept $\Delta H^o_{ads}$ and $\Delta S^o_{ads}$ can be calculated.

It can be noticed that the $\Delta H^o_{ads}$ value is negative, referring that the BZ molecules′ adsorption on the MS surface is an exothermic process. This also explains the reduction in the BZ molecules adsorption affinity with increasing the temperature. Nevertheless, the $\Delta S^o_{ads}$ values are positive, which is ascribed to the increase in the solvent energy and the substitution of the $H_2O$ molecules with the inhibitor one [45]. Additionally, calculating the entropy change of adsorption based on the enthalpy and the free energy change of adsorption would give better knowledge for the random molecule movement of BZ corrosion inhibitor on the MS surface as mentioned in the equation below [46].

$$\Delta G^o_{ads} = \Delta H^o_{ads} - T\Delta S^o_{ads} \tag{15}$$

### 3.4 Thermodynamic Activation Parameter

The influence of temperature on the electrochemical processes rate, the adsorption equilibrium, and kinetics of MS in aggressive media without and with adding different concentrations of BZ is shown in Figure S5. Herein, the thermodynamic activation parameters such as the activation energy $E_a$, the activation enthalpy $\Delta H_a$ and the

  

activation entropy $\Delta S_a$ were derived from the Arrhenius and the transition state equations [47].

$$CR = Aexp\left(^{-E_a}/_{RT}\right) \quad (16)$$

where $CR$ is the experimental corrosion rate of obtained from the polarization test at absolute temperature, $A$ is the Arrhenius pre-exponential factor related to the metal and the electrolyte type, and $E_a$ is the estimated activation energy, and $R$ is the universal gas constant.

Figure S5 exhibits the linear relationship between log $CR$ versus 1/T. The slopes with best-fitting regression lines are attributed to the apparent activation energy ($E_a$) at a definite concentration as represented in Table 4.

It can be noticed that the higher the BZ corrosion inhibitor concentration, the more activation energy is calculated as an evident indication for the physisorption process. This is ascribed to the BZ corrosion inhibitor molecule's strong affinity to be adsorbed on the metal surface by blocking the MS substrate's charge transfer and prohibiting the corrosion reaction [48]. Additionally, the $E_a$ values in the absence and the presence of BZ concentrations are greater than 20 kJ/mol which reveals that the surface reaction is the dominant process in the corrosion mechanism. Overall, the adsorption phenomenon of an organic molecule could possess a wide range of interactions based on the experimental results [49].

On the other hand, the activation enthalpy $\Delta H_a$ and the activation entropy $\Delta S_a$ were calculated according to the transition state equation as seen below

$$CR = \left(^{RT}/_{N_A h}\right) exp\left(^{\Delta S_a}/_{R}\right) exp\left(^{-\Delta H_a}/_{RT}\right) \quad (17)$$

where $CR$ stands for the corrosion rate at absolute temperature $T$, R is the ideal gas constant, $N_A$ refers to Avogadro's number ($6.022\times10^{23}$ mol$^{-1}$), and $h$ corresponds to Plank's constant ($6.626\times10^{-34}$ J.s).

Figure S6 displays a relation between log $(\frac{CR}{T})$ versus the absolute temperature reciprocal of MS exposed to 0.5 M $H_2SO_4$ without and with adding various dosages from the BZ corrosion inhibitor. The attained slope corresponding to $\frac{-\Delta H_a}{2.303R}$ and the intercept refers to $(\log\frac{R}{Nh}+\frac{\Delta S_a}{2.303R})$. the obtained values of $\Delta H_a$ and $\Delta S_a$ are tabulated in Table 4. It can be noticed that the values of $\Delta H_a$ shift to the positive direction with increasing the BZ concentration. This is attributed to the difficulty of the MS corrosion in the BZ solutions [50]. Additionally, the $\Delta S_a$ values shift to the more positive direction in the presence of the BZ inhibitor which implies that the corrosion system shift to the near-equilibrium state with an increase in the BZ concentration [51]. Moreover, the average difference between the activation energy and the activation enthalpy is 2.66 KJ/mol, which is almost equal to 2.61 KJ/mol, shown in the equation below. This indicates that the corrosion process is a unimolecular reaction.

$$RT = E_a - \Delta H_a \quad (18)$$

Table 4. Activation and thermodynamic parameters from Arrhenius and transition state equations for the MS in the absence and the presence of different concentrations of the BZ corrosion inhibitor.

| Conc. of inhibitor (M) | $E_a$ (kJ/mol) | $\Delta H_a$ (kJ/mol) | $\Delta S_a$ (kJ/mol) |
|---|---|---|---|
| Blank | 80.94 | 78.32 | 133.19 |
| $5\times10^{-5}$ | 117.23 | 114.59 | 242.09 |
| $1\times10^{-4}$ | 122.67 | 119.99 | 254.91 |
| $5\times10^{-4}$ | 125.15 | 122.5 | 259.89 |
| $1\times10^{-3}$ | 129.46 | 126.83 | 268.31 |
| $5\times10^{-3}$ | 133.59 | 130.86 | 275.20 |

### 3.5 Synergism BZ and Iodide Ions

The synergistic effects of adding 1 mM of KI to the different concentrations of BZ can be seen from the polarization behavior of MS in 0.5 M $H_2SO_4$ at 20 °C, Figure S7A. The corrosion parameters derived from the curves are listed in Table S2. They show that the combination of BZ and KI reduced the anodic and cathodic reactions and resulted in a decrease in the corrosion current densities compared to the corresponding cases when a solution with BZ exists alone. For example, it increases the corrosion inhibition efficiency by up to 91.38 % compared to 81 % at $5\times10^{-4}$ M of BZ. The KI addition affects the adsorption film resistance of the BZ corrosion inhibitor, as is also confirmed by the EIS measurements displayed in the Nyquist plot of MS in 0.5 M $H_2SO_4$ at 20 °C, as shown in Figure S7B.

The diameters of the semicircles increase with the addition of KI. The electrochemical parameters obtained from fitting the Nyquist plot using the equivalent circuit in Figure S1 are given in Table S3. The $R_{ct}$ increased from 33 to 71 Ω cm$^2$ in the blank and with 1 mM KI solutions, respectively. Meanwhile, the $R_{ct}$ values are doubled from 119 to 243.9 Ω cm$^2$ without and with adding one mM KI to $5\times10^{-5}$ M BZ solution, respectively. The enhanced inhibition efficiency noted for BZ on the addition of $I^-$ is attributed to the integrative adsorption as the anion ($I^-$) compete with the other anions for getting adsorbed on the MS active sites, then the adsorbability of the BZ molecules is enhanced by the electrostatic interaction with the adsorbed ($I^-$), resulting in interconnected paths between the BZ corrosion inhibitor and the MS substrate [52,53].

The synergistic parameter ($S_i$) is measured from the inhibition efficiency values obtained from both potentiodynamic polarization and EIS methods according to the equation below [54]

  

$$S_i = \frac{1 - I_{KI+BZ}}{1 - I'_{KI+BZ}} \quad (19)$$

where $I_{KI+BZ} = I_{KI} + I_{BZ}$, $I_{KI}$, and $I_{BZ}$ are the inhibition efficiency of $I^-$ ions and the BZ inhibitor, respectively. $I'_{KI+BZ}$, is the inhibition efficiency of the BZ inhibitor when combined with $I^-$ ions [42].

Table 5. The synergism parameter ($S_i$) for different BZ concentrations in the presence of 1 mM KI.

| Concentration, M | Synergism parameter, $S_i$ EIS | Potentiodynamic |
|---|---|---|
| $5\times10^{-5}$ | 1.46 | 1.84 |
| $1\times10^{-4}$ | 1.53 | 1.82 |
| $5\times10^{-4}$ | 1.56 | 1.84 |
| $1\times10^{-3}$ | 1.55 | 1.86 |
| $5\times10^{-3}$ | 1.56 | 1.87 |

The $S_i$ values obtained are listed in Table 5. It is worth mentioning that KI is commonly used as a synergism for many other inhibitors. However, the synergism mechanism is changeable based on $S_i$ values. If the $S_i$ value approaches the unity, no interaction between the inhibitor compounds exist. Meanwhile, $S_i > 1$ refers to a synergistic effect. When $S_i < 1$, this means that the antagonistic interaction is permanent, which may be attributed to competitive adsorption [55]. Table 5 shows that the synergistic parameter ($S_i$) for the iodide ions is higher than unity. This confirms that the enhanced inhibition efficiency is caused by the addition of iodide ions to the BZ inhibitor is due to a synergistic effect [56,57].

### 3.6 Effect of Immersion Time

Figure 5 shows the effect of the immersion time of MS in 0.5 M $H_2SO_4$ + the optimum concentration of BZ ($5\times10^{-3}$) in the absence (Figure 5A) and the presence of 1 mM of KI (Figure 5B) on the electrochemical impedance spectra, which are measured every 30 minutes. It can be seen in Table S4 that the surface coverage of the BZ corrosion inhibitor increases with increasing the immersion time for three hours. Then a slight reduction is noticed after 210 minutes of immersion. Meanwhile, the presence of the $I^-$ ions on the protective layer is not significant with time [58].

### 3.7 Potential of Zero Charge Analysis

The potential of zero charge (PZC) is a significant fundamental phenomenon in surface science related to the concept of adsorption under zero electric charge of the substrate. The surface charge would be identified by the value of the open circuit potential versus the pzc value. Figure 6 represents the obtained double-layer capacitance $C$ at different potential values at 100 Hz. It

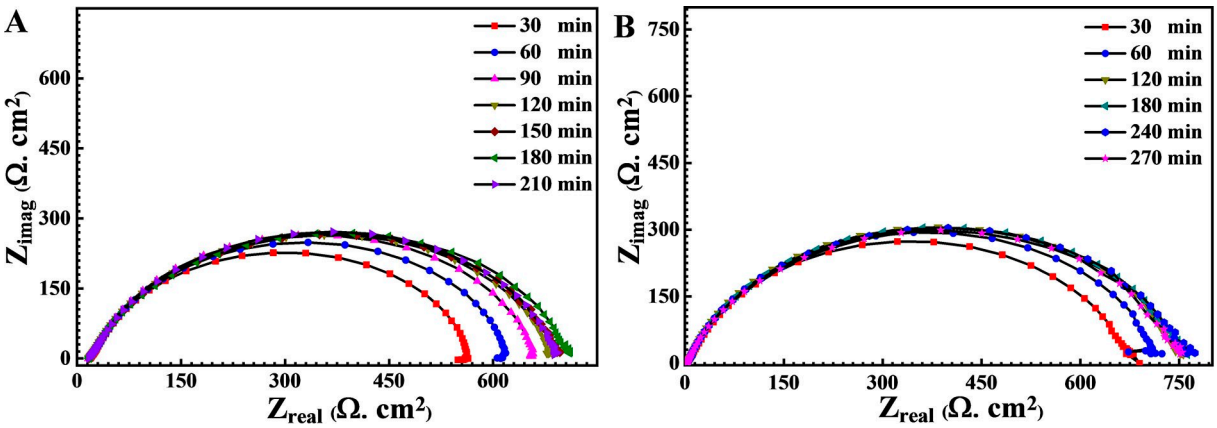


Fig. 5. Nyquist plots for MS after different immersion times in A) 0.5 M $H_2SO_4 + 5\times10^{-3}$ M BZ and B) 0.5 M $H_2SO_4 + 5\times10^{-3}$ M BZ + 1 mM KI.

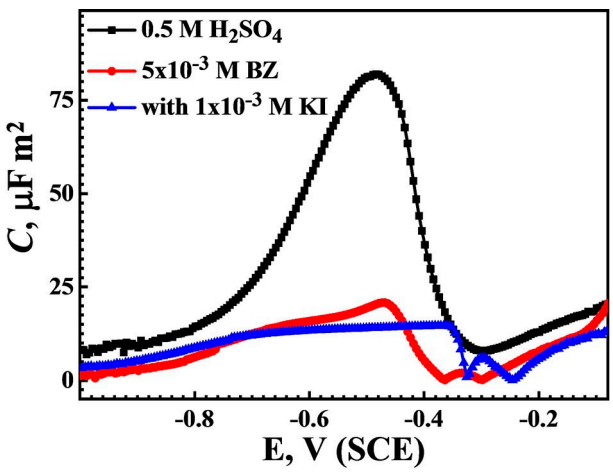


Fig. 6. The estimated $C$ versus the applied potential for MS exposed to 0.5 M $H_2SO_4$ without and with $5\times10^{-3}$ M BZ in the absence and the presence of $1\times10^{-3}$ KI.

  

can be noticed that the C value significantly decreases by adding the optimum concentration of the BZ corrosion inhibitor. Moreover, adding 1 mM KI to the tested solution reduces the capacitance value.

Additionally, the PZC and the OCP values were presented in Table S5. Interestingly, the maximum capacitance can be seen at −0.487 V, which can be named PZC of MS in 0.5 M $H_2SO_4$. The $E_{ocp}$ in the same conditions was −0.509 V. It indicates a positively charged MS surface at OCP, which is attributed to the metal substrate's anodic dissolution. Meanwhile, the presence of $5\times10^{-3}$ M of BZ corrosion inhibitor shifts the PZC value to a more positive value of −0.462 V SCE. It could be corresponding to the protonation of the BZ molecules in an acidic medium, which influences the BZ adsorption via the electrostatic interactions [59]. Furthermore, the synergistic effect of 1 mM of KI in the tested solution is also reflected in the PZC value as it was substantially decreased to −0.350 V vs. SCE, which is attributed to the competing effect of the $I^-$ ions on adsorption on the MS surface versus the aggressive ions which enhance the BZ molecules adsorbability [60].

### 3.8 Surface Morphology Studies

Figure 7 displays the SEM surface analysis before and after the corrosion in 0.5 M $H_2SO_4$, without and with adding $5\times10^{-3}$ M of BZ, respectively, in the absence and the presence of 1 mM KI after two hours of exposure. The SEM micrograph of the surface of MS in the inhibitor-free solution is shown in Figure 7A. It shows a heterogeneous layer of corrosion products. Additionally, the optical profilometry reveals the MS surface topography in three-dimensional, as shown in Figure S8. The optical profilometer image for the MS in the aggressive solution Figure S8B shows the high surface roughness (1373 nm) due to the corrosion product layer formation. On the other side, in the inhibited MS with $5\times10^{-3}$ M BZ, the SEM micrograph demonstrated in Figure 7A for MS shows a large surface area of MS free from any corrosion products. As in Figure S8C, the optical profilometer shows a reduction in MS surface roughness (50 nm). The SEM micrograph of MS in the presence of 1 mM KI and $5\times10^{-3}$ M BZ at high magnification power 10000× displays a smoother surface with little corrosion product over the MS, and this is confirmed by the optical profilometer 3-D image, which displays a significant reduction in the surface roughness (20 nm). These observations are additional proofs regarding the Schiff base's high corrosion inhibition efficiency and the synergistic effects of iodide ions.

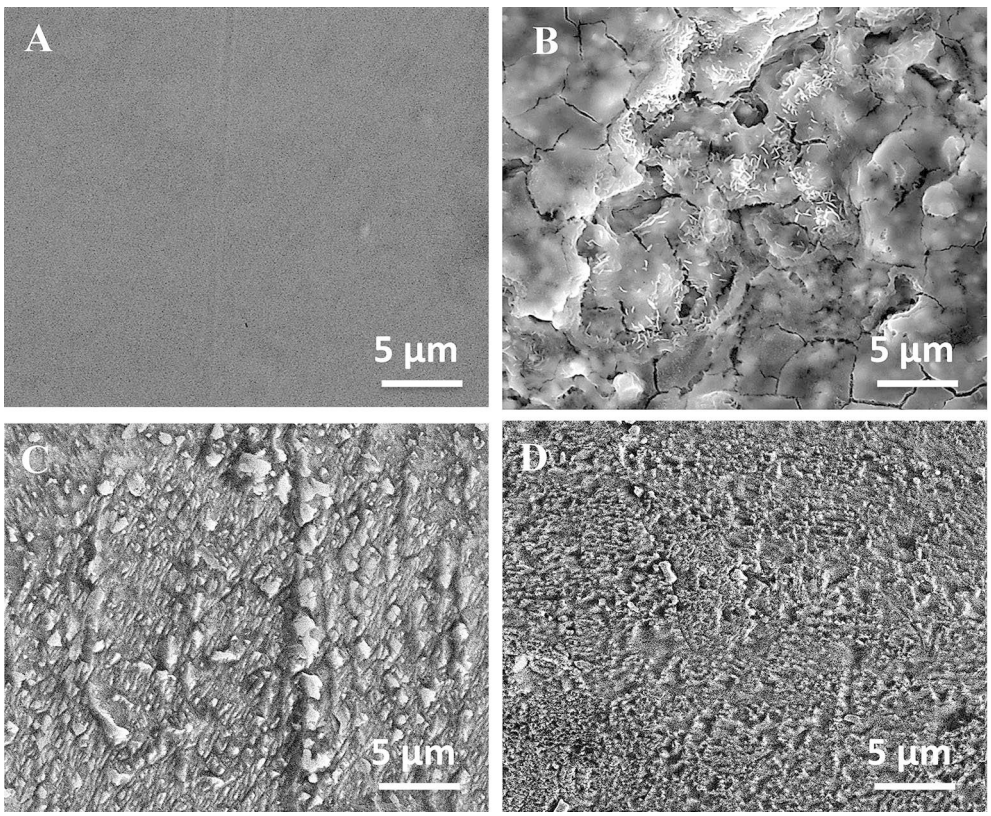


Fig. 7. SEM micrographs for MS surface of immersion for 12 hr. in a) 0.5 M $H_2SO_4$, (b) in the presence of $5\times10^{-3}$ M BZ, (c) 0.5 M $H_2SO_4+5\times10^{-3}$ M BZ + 1 mM KI, at 20 °C.

  

### 3.9 Quantum Calculations Study

The electronic quantum parameters for the investigated Schiff base (BZ) including the energy of the highest occupied molecular orbital ($E_{HOMO}$), the energy of the lowest unoccupied molecular orbital ($E_{LUMO}$), the difference between LUMO, and HOMO (energy gap, $\Delta E$) are calculated and discussed in gaseous and aqueous phases to understand the corrosion inhibition mechanism of the BZ corrosion inhibitor. The corrosion inhibition performance of the prepared Schiff base molecules is based on the adsorption phenomenon related to the donor-acceptor interactions between the high electron density centers in the inhibitor molecule (π-electrons, S and N hetero atoms) and vacant d orbitals of the Fe atom. The frontier HOMO and LUMO orbitals in the optimized structures and the inhibitor are shown in Figures 8 and 9.

The $E_{HOMO}$ is −4.75 eV and −4.99 eV in the gaseous and aqueous phase, respectively, reflects the tendency of the BZ molecules to donate electrons to vacant 3d-orbital of Fe, while the $E_{LUMO}$ (0.869 eV) displays its ability to accept electrons from the 4S-orbitals of Fe atoms. The high value of $\Delta E$ (8.619 eV) reflects the metal ion complex's stability over the MS surface, leading to an increase in the corrosion inhibition efficiency when the Schiff base compound is used [61,62]. The calculated value of the fraction electron transfer ($\Delta N$) value is compatible with Lukovit's study.

The $\Delta N$ value is 0.412, i.e., less than 3.6, suggests that the inhibition efficiency increases with increasing electron-donating ability of the BZ to MS surface [63]. Therefore, these results are in good agreement with the obtained experimental data, i.e., the inhibitor molecules favor the chemical adsorption dictated by the physical interaction (chemi/physisorption) on the MS surface. Furthermore, the reactive sites for the electrophilic and nucleophilic reactions can be detected using the molecular electrostatic potential (MEP) mapping technique [64]. Figure 9 shows the molecular electrostatic potential (MEP) map of the insight compound, indicating the high and/or the low electron density regions (nucleophilic and electrophilic attack). It can be seen out from the MEP map that the heteroatoms (S and N) and the π- electrons (Thiazol ring and imine group) have an excess negative charge that enhanced the adsorption process and the formation of a protective layer over the Fe surface, which increased the corrosion inhibition efficiency of BZ over MS in the 0.5 M $H_2SO_4$ solution.

### 3.10 Monte Carlo Simulation Study

Quantum chemical calculations provide crucial details about the inhibition mechanism, the influence of the corrosive ions still under debate [65]. Consequently, the necessity for modeling a method to mimic the interaction of the inhibitor molecule with the metal substrate in the presence of aggressive ions and real conditions. Metropolis Monte Carlo technique was employed to search for the most stable low energy adsorption configurations of the inhibitor molecule on Fe (110) atoms in the vacuum and water in the presence of hydronium and sulfate ions as presented in Figure 10. It depicts the top and side views

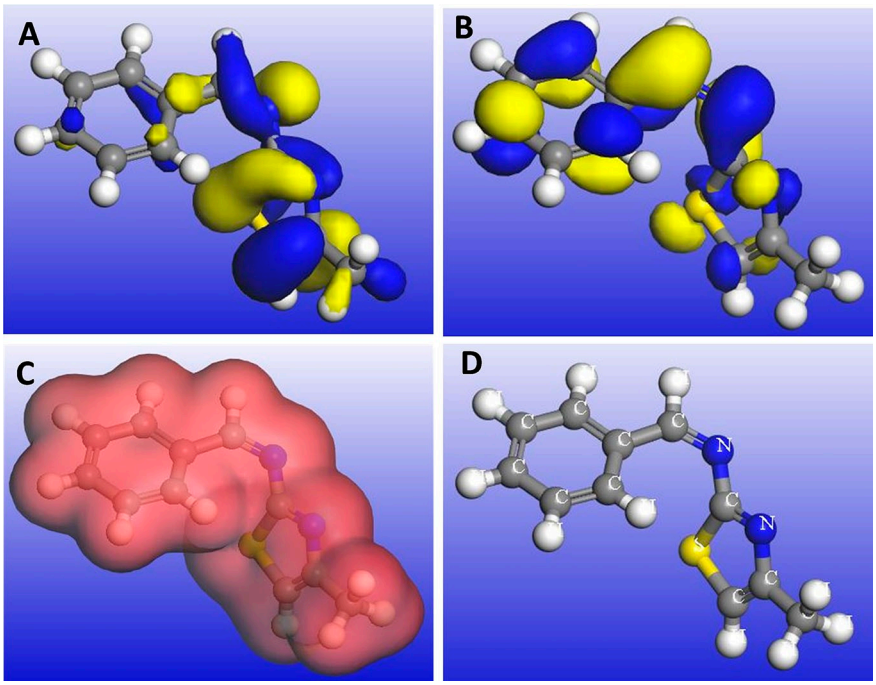


Fig. 8. A) HOMO, B) LUMO, C) electrostatic potential map, and D) the optimized structure obtained by DFT analysis for the BZ compound in the aqueous phase.

  

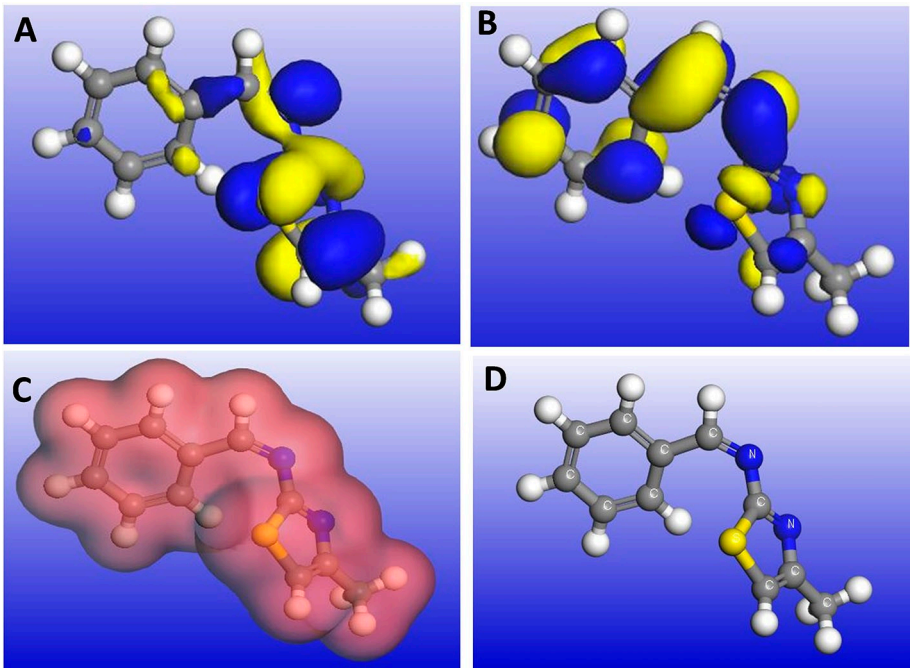


Fig. 9. A) HOMO, B) LUMO, C) electrostatic potential map, and D) the optimized structure obtained by DFT analysis for the BZ compound in the gas phase.

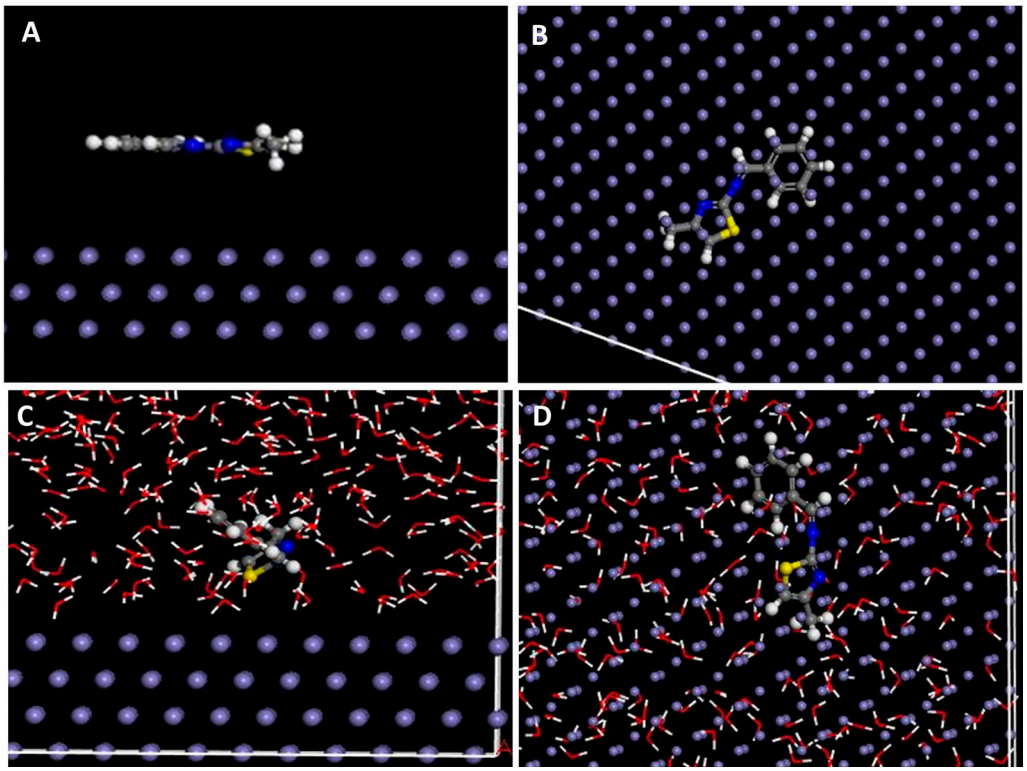


Fig. 10. Side view and top view equilibrium adsorption configurations of the BZ corrosion inhibitor in gas phase (A, B) and aqueous phase (C, D).

of the BZ Schiff base's stable configurations in the gaseous and aqueous phases to be adsorbed in Fe (110) surface. The outputs of simulation energies were listed in Table 6. It includes total energy ($E_{Tot}$) which represents the summation of the internal and the adsorption energy of the adsorbate, the adsorption energy ($E_{ads}$) correspond-

  

Table 6. Quantum chemical parameters of the compounds based on (DNP) basis set.

| BZ | $E_{HOMO}$ | $E_{LUMO}$ | $\Delta E$ | $A$ | $I$ | $X$ | $\eta$ | $\Delta N$ | $\mu$ |
|---|---|---|---|---|---|---|---|---|---|
| Gas | −4.70 | −2.54 | 2.15 | 2.54 | 4.70 | 3.62 | 1.07 | 1.56 | 3.70 |
| Aqueous | −4.99 | −2.66 | 2.32 | 2.66 | 4.99 | 3.82 | 1.16 | 1.36 | 5.27 |

ing to the released energy from the interaction of the adsorbate with the MS substrate and equal the summation of $(E_{Rigid})$ and $(E_{DEf})$. The rigid adsorption energy $(E_{Rigid})$ refers to the released or the required energy for a non-optimized adsorbate to be adsorbed on the MS surface, while the deformation energy $(E_{DEf})$ is the released energy from the relaxation of the adsorbed molecules on the MS substrate [66]. It is worthy of mentioning here that the inhibitor's effectiveness can be determined theoretically as it is directly proportional to the adsorption energy [67]. It can be noticed in Table 7 that all energies values in the aqueous phase are more negative than their counterparts in the gaseous phase.

## 4 Conclusion

The potentiodynamic polarization measurements prove that the BZ inhibitor is of the mixed-type category and the corrosion rate decreases as the concentration of BZ increases. The EIS data also confirms the potentiodynamic polarization results, and the inhibition efficiency reaches 95 % for the optimum concentration of the BZ inhibitor ($5\times10^{-3}$ M) at 20 °C. The BZ inhibitor increases the charge transfer resistance and decreases the $C_{dl}$ values due to its adsorption on the MS surface instead of the water molecules. Furthermore, the values of the standard adsorption free energy change ($\Delta G^{o}_{ads}$) and activation energy ($E_a$) indicates the strong adsorption tendency of the inhibitor. Also, the addition of KI has a synergetic effect on the BZ corrosion inhibition efficiency, where the synergistic parameter ($S_i$) is greater than unity. The potential of zero charge measurements revealed that the MS is positively charged at OCP in the presence of the BZ inhibitor and $I^-$ ions. Besides, $E_{HOMO}$ and the $\Delta N$ parameters are further proof of the inhibition action of the BZ Schiff base compound. Finally, the Monte Carlo simulation approach confirmed the correlation between both the experimental and theoretical results.

## Acknowledgments

This publication was made possible by an NPRP award [NPRP10-0125-170252] from the Qatar National Research Fund (a member of The Qatar Foundation). The statements made herein are solely the responsibility of the author[s]." The authors also thank the Central Lab Unit at Qatar University for obtaining the SEM images presented in this work. Open Access funding provided by the Qatar National Library.

## Data Availability Statement

The data will be available upon request.

## References

[1] K. Mallaiya, R. Subramaniam, S. S. Srikandan, S. Gowri, N. Rajasekaran, A. Selvaraj, *Electrochim. Acta* **2011**, *56*, 3857–3863.
[2] M. A. Amin, K. F. Khaled, Q. Mohsen, H. A. Arida, *Corros. Sci.* **2010**, *52* 1684–1695.
[3] W. Yang, Q. Wang, K. Xu, Y. Yin, H. Bao, X. Li, L. Niu, S. Chen, *Materials* **2017**, *10*, 956 .
[4] A. A. Abd-Elaal, N. M. Elbasiony, S. M. Shaban, E. G. Zaki, *J. Mol. Liq.* **2018**, *249*, 304–317.
[5] I. A. Zaafarany, *Int. J. Corros. Scale Inhib.* **2014**, *3*, 12–27.
[6] D. Daoud, T. Douadi, S. Issaadi, S. Chafaa, *Corros. Sci.* **2014**, *79*, 50–58.
[7] I. Ahamad, R. Prasad, M. A. Quraishi, *Corros. Sci.* **2010**, *52*, 1472–1481.
[8] A. A. Farag, A. S. Ismail, M. A. Migahed, *J. Mol. Liq.* **2015**, *211*, 915–923.
[9] M. Prajila, A. Joseph, *J. Mol. Liq.* **2017**, *241*, 1–8.
[10] B. R. Zhang, C. J. He, C. Wang, P. D. Sun, F. T. Li, Y. Lin, *Corros. Sci.* **2015**, *94*, 6–20.
[11] G. Eyu, G. Will, W. Dekkers, J. MacLeod, *Materials* **2016**, *9*, 868.
[12] H. Vashisht, I. Bahadur, S. Kumar, M. S. Goyal, G. Kaur, G. Singh, L. Katata-Seru, E. E. Ebenso, *J. Mol. Liq.* **2016**, *224*, 19–29.
[13] M. A. M. El-Haddad, A. Bahgat Radwan, M. H. Sliem, W. M. I. Hassan, A. M. Abdullah, *Sci. Rep.* **2019**, *9*, 3695.
[14] M. H. Sliem, M. Afifi, A. Bahgat Radwan, E. M. Fayyad, M. F. Shibl, F. E.-T. Heakal, A. M. Abdullah, *Sci. Rep.* **2019**, *9*, 2319.
[15] D. Q. Zhang, L. X. Gao, G. D. Zhou, *J. Appl. Electrochem.* **2003**, *33*, 361–366.
[16] S. A. Umoren, Y. Li, F. H. Wang, *Corros. Sci.* **2010**, *52*, 2422–2429.
[17] I. M. Gadala, A. Alfantazi, *Appl. Surf. Sci.* **2015**, *357*, 356–368.
[18] A. Fattah-alhosseini, *Arab. J. Chem.* **2016**, *9*, S1342-S1348.

Table 7. Outputs and descriptors calculated by Monte Carlo simulation for the lowest adsorption configurations of BZ corrosion inhibitor in gas and aqueous phase on Fe(110).

| BZ phase | $E_{Tot}$ (kJ/mol) | $E_{ads}$ (kJ/mol) | $E_{Rigid}$ (kJ/mol) | $E_{Def}$ (kJ/mol) | $dE_{ads}/dNi$ (kJ/mol) |
|---|---|---|---|---|---|
| Gas phase | −0.131 | −0.165 | −0.109 | −0.055 | −165.353 |
| Aqueous phase | −42.1 | −51.8 | −44.2 | −7.62 | −219.361 |

  

[19] Y. Sasikumar, A. S. Adekunle, L. O. Olasunkanmi, I. Bahadur, R. Baskar, M. M. Kabanda, I. B. Obot, E. E. Ebenso, *J. Mol. Liq.* **2015**, *211*, 105–118.
[20] C. Verma, M. A. Quraishi, K. Kluza, M. Makowska-Janusik, L. O. Olasunkanmi, E. E. Ebenso, *Sci. Rep.* **2017**, *7*, 44432.
[21] I. B. Obot, I. B. Onyeachu, A. M. Kumar, *Carbohyd. Polym.* **2017**, *178*, 200–208.
[22] M. A. Migahed, A. A. Farag, S. M. Elsaed, R. Kamal, M. Mostfa, H. A. El-Bary, *Mater. Chem. Phys.* **2011**, *125*, 125–135.
[23] C. Verma, A. A. Sorour, E. E. Ebenso, M. A. Quraishi, *Results Phys* **2018**, *10*, 504–511.
[24] O. Kaczerewska, R. Leiva-Garcia, R. Akid, B. Brycki, I. Kowalczyk, T. Pospieszny, *J. Mol. Liq.* **2018**, *249*, 1113–1124.
[25] S. Y. A. E. Kowsari, M. H. Shahini, H. Zandi, A. Ehsani, R. Naderi, A. PourghasemiHanza, M. Mehdipour, *Corros. Sci.* **2016**, *112*, 73–85.
[26] M. Mobin, M. Rizvi, *Carbohyd. Polym.* **2017**, *156*, 202–214.
[27] A. Y. E.-E. M. A. Hegazy, M. El-Shafaie, K. M. Berry, *J. Mol. Liq.* **2016**, *214*, 347–356.
[28] M. A. Bedair, M. M. B. El-Sabbah, A. S. Fouda, H. M. Elaryian, *Corros. Sci.* **2017**, *128*, 54–72.
[29] S. Abd El Wanees, N. M. ElBasiony, A. M. Al-Sabagh, M. A. Alsharif, S. M. Abd El Haleem, M. A. Migahed, *J. Mol. Liq.* **2017**, *248*, 943–952.
[30] S. M. Shaban, R. M. El-Sherif, M. A. Fahim, *J. Mol. Liq.* **2018**, *252*, 40–51.
[31] H. Heydari, M. Talebian, Z. Salarvand, K. Raeissi, M. Bagheri, M. A. Golozar, *J. Mol. Liq.* **2018**, *254*,177–187.
[32] M. Mobin, M. Rizvi, *Carbohyd. Polym.* **2016**, *136*, 384–393.
[33] N. J. N. Nnaji, O. T. Ujam, N. E. Ibisi, J. U. Ani, T. O. Onuegbu, L. O. Olasunkanmi, E. E. Ebenso, *J. Mol. Liq.* **2017**, *230*, 652–661.
[34] P. C. Okonkwo, M. H. Sliem, R. A. Shakoor, A. M. A. Mohamed, A. M. Abdullah, *J. Mater. Eng. Perform.* **2017**, *26*, 3775–3783.
[35] Y. Tang, F. Zhang, S. Hu, Z. Cao, Z. Wu, W. Jing, *Corros. Sci.* **2013**, *74*, 271–282.
[36] B. J. Usman, S. A. Umoren, Z. M. Gasem, *J. Mol. Liq.* **2017**, *237*, 146–156.
[37] R. Kumar, O. S. Yadav, G. Singh, *J. Mol. Liq.* **2017**, *237*, 413–427.
[38] R. Kumar, R. Chopra, G. Singh, *J. Mol. Liq.* **2017**, *241*, 9–19.
[39] T. K. Chaitra, K. N. S. Mohana, H. C. Tandon, *J. Mol. Liq.* **2015**, *211*, 1026–1038.
[40] A. Samide, E. G. Iacobescu, B. Tutunaru, R. Grecu, C. Tigae, C. Spînu, *Coatings* **2017**, *7*, 181.
[41] A. B. Radwan, M. H. Sliem, N. S. Yusuf, N. A. Alnuaimi, A. M. Abdullah, *Sci. Rep.* **2019**, *9*, 18115.
[42] S. S. Durodola, A. S. Adekunle, L. O. Olasunkanmi, J. A. O. Oyekunle, *Electroanalysis* **2020**, doi.org/10.1002/elan.202060227 .
[43] A. Dutta, S. K. Saha, U. Adhikari, P. Banerjee, D. Sukul, *Corros. Sci.* **2017**, *123*, 256–266.
[44] E. A. Badr, M. A. Bedair, S. M. Shaban, *Mater. Chem. Phys.* **2018**, *219*, 444–460.
[45] I. B. Obot, S. A. Umoren, Z. M. Gasem, R. Suleiman, B. E. Ali, *J. Ind. Eng. Chem.* **2015**, *21*, 1328–1339.
[46] A. Bahgat Radwan, M. H. Sliem, P. C. Okonkwo, M. F. Shibl, A. M. Abdullah, *J. Mol. Liq.* **2017**, *236*, 220–231.
[47] A. D. Becke, *J. Chem. Phys.* **1993**, *98*, 5648.
[48] J. H. Al-Fahemi, M. Abdallah, E. A. M. Gad, B. A. A. L. Jahdaly, *J. Mol. Liq.* **2016**, *222*, 1157–1163.
[49] K. Shahzad, M. H. Sliem, R. A. Shakoor, A. B. Radwan, R. Kahraman, M. A. Umer, U. Manzoor, A. M. Abdullah, *Sci. Rep.* **2020**, *10*, 4314.
[50] N. Anusuya, J. Saranya, P. Sounthari, A. Zarrouk, S. Chitra, *J. Mol. Liq.* **2017**, *225*, 406–417.
[51] A. Bousskri, A. Anejjar, M. Messali, R. Salghi, O. Benali, Y. Karzazi, S. Jodeh, M. Zougagh, E. E. Ebenso, B. Hammouti, *J. Mol. Liq.* **2015**, *211*, 1000–1008.
[52] K. M. Ramya, R. Anupama, K. K. Joseph, *Mater. Chem. Phys.* **2015**, *150*, 632–647.
[53] N. T. Zhe Zhanga, X. Lia, L. Zhanga, L. Wuc, Y. Huanga, *Appl. Surf. Sci.* **2015**, *357*, 845–855.
[54] I. O. Arukalam, *Carbohyd. Polym.* **2014**, *112*, 291–299.
[55] S. A. Umoren, O. Ogbobe, I. O. Igwe, E. E. Ebenso, *Corros. Sci.* **2008**, *50*, 1998–2006.
[56] P. C. Okafor, Y. Zheng, *Corros. Sci.* **2009**, *51*, 850–859.
[57] A. A. Farag, M. A. Hegazy, *Corros. Sci.* **2013**, *74*, 168–177.
[58] M. S. J. A. Fattah-alhosseini, *J. Alloys Comp.* **2015**, *646*, 685–691.
[59] A. Ongun Yüce, B. Doğru Mert, G. Kardaş, B. Yazıcı, *Corros. Sci.* **2014**, *83*, 310–316.
[60] B. D. Mert, M. Erman Mert, G. Kardaş, B. Yazıcı, *Corros. Sci.* **2011**, *53*, 4265–4272.
[61] K. R. A. Parul Dohare, M. A. Quraishi, I. B. Obot, *J. Ind. Eng. Chem.* **2017**, *52*, 197–210.
[62] A. M. Al-Sabagh, M. A. Migahed, S. A. Sadeek, N. M. El Basiony, *Egypt. J. Pet.* **2018**, doi.org/10.1016/j.ejpe.2017.12.003.
[63] H. M. Abd El-Lateef, A. M. Abu-Dief, M. A. A. Mohamed, *J. Mol. Struct.* **2017**, *1130*, 522–542.
[64] A. e. Fouda, A. Abd El-Aal, M. Sliem, A. Abdullah, *Egypt. J. Chem.* **2020**, *63*, 759–776.
[65] D. Zhang, Y. Tang, S. Qi, D. Dong, H. Cang, G. Lu, *Corros. Sci.* **2016**, *102*, 517–522.
[66] A. Zeino, I. Abdulazeez, M. Khaled, M. W. Jawich, I. B. Obot, *J. Mol. Liq.* **2018**, *250*, 50–62.
[67] P. Kannan, A. Varghese, K. Palanisamy, A. S. Abousalem, *J. Mol. Liq.* **2020**, *297*, 111855.

Received: October 20, 2020
Accepted: October 22, 2020
Published online on November 10, 2020

  